**Indonesian Journal of Electrical Engineering and Computer Science**
Vol. 43, No. 1, July 2026, pp. 192~206
ISSN: 2502-4752, DOI: 10.11591/ijeecs.v43.i1.pp192-206 

# A hybrid approach for multi-view MRI Alzehimer's detection using convolutional neural networks and bio-inspired algorithms

**Iheb Chemss El Dine Hagani[1], Nacéra Benamrane[1], Lakhdar Sais[2]**
[1]SIMPA Laboratory, Department of Informatics, University of Sciences and Technology of Oran - Mohamed Boudiaf, Oran, Algeria
[2]Centre de Recherche en Informatique de Lens (CRIL), CNRS, Université d'Artois, Lens, France

**Article Info**

***Article history:***

Received Mar 23, 2026
Revised Jun 22, 2026
Accepted Jun 29, 2026

***Keywords:***

Alzheimer's disease
Bio-inspired optimization
Convolutional neural networks
Genetic algorithm
MRI
Particle swarm optimization

**ABSTRACT**

Alzheimer's disease (AD) is a neurodegenerative disorder that remains incurable to date. Therefore, the most important step in treatment remains the early detection of the signs indicating its presence. The sooner these signs are discovered, the sooner preventative care can be administered. Convolutional neural networks (CNNs) have demonstrated impressive performance in medical image analysis; however, they often suffer from suboptimal manual tuning of their hyperparameters. Therefore, we opted for a hybrid method combining them with genetic algorithms (GA) and particle swarm optimization (PSO) to automatically optimize architectures and fusion weights for improved AD detection. Using data obtained from ADNI and Kaggle, our approach achieved 87.4% accuracy, surpassing classical CNNs of the same size and depth. These results highlight the potential of evolutionary optimization for developing reliable diagnostic tools.



***Corresponding Author:***

Iheb Chemss El Dine Hagani
SIMPA Laboratory, Department of Informatics
University of Sciences and Technology of Oran - Mohamed Boudiaf
Oran, Algeria
Email: ihebchemsseldine.hagani@univ-usto.dz

## 1. INTRODUCTION

Alzheimer's disease (AD) presents a significant challenge for modern medicine, and magnetic resonance imaging (MRI) remains the modality of choice for clinicians. However, manual analysis of MRIs is a time-consuming task. This is why this decade has seen the emergence of artificial intelligence (AI) applications in the medical field in general, and more specifically in imaging. Deep learning (DL), a subset of AI, more specifically convolutional neural network (CNN), has revolutionized image analysis and, consequently, medical image analysis. By automating certain steps such as feature extraction, segmentation and classification [1]-[5], these tools have allowed specialists to focus their expertise on interpreting results, early detecting subtle abnormalities, and developing a personalized care plan for the patient. Despite their success, CNN-based approaches for AD classification face two persistent limitations. First, architectures and hyperparameters are typically designed through manual trial-and-error, a costly and non-reproducible process that restricts the exploration of the design space. Second, when predictions from multiple anatomical views are combined, uniform averaging is commonly applied rather than a data-driven weighting scheme-an approach that disregards the varying discriminative power of each orientation. Before the advent of CNNs, bio-inspired approaches had already demonstrated the potential of such optimization in the medical field. Genetic algorithms (GA) [6], [7] and particle swarm optimization (PSO) [8] offer a multitude of possible applications [9], [10]. Based on these observations, we propose a hybridization of CNNs with GA and PSO,

extending a preliminary study [11] that combined CNNs with PSO for Alzheimer's detection. The key contribution of this work is twofold: (i) GA automates the search for CNN architectures adapted to each anatomical orientation, removing the need for manual design; and (ii) PSO is employed not as a network weight optimizer but to determine optimal fusion weights for combining orientation-specific predictions - a novel application of PSO to the multi-view fusion problem. We chose to work with 2D slices extracted from 3D volumes. This choice was facilitated by the lower computational cost of 2D architectures, a decisive factor within the GA optimization loop where numerous candidate models are trained iteratively. More fundamentally, the multi-view approach itself is built around the 2D representation: decomposing each volume into axial, coronal, and sagittal slices is precisely what yields the three distinct views that PSO subsequently weights and fuses. A volume processed directly by a single 3D network would expose no separate orientations to combine, and the fusion mechanism at the core of our contribution would lose its object. As indicated in the title, "multi-view" thus refers to the three principal anatomical planes (axial, coronal, and sagittal). In section 2 then details the proposed hybrid methodology. Section 3. presents and analyzes the experimental results, and section 4. draws conclusions and outlines directions for future research.

## 2. RELATED WORK

For several years now, the application of DL has reached the expansion stage in the field of medical image analysis. Among the most widely used models are convolutional neural networks, demonstrating unprecedented potential. In 2025, a comprehensive review of DL techniques for the detection of AD highlighted that *"CNNs are consistently found to outperform traditional ML approaches, showcasing their potential in improving diagnostic accuracy"* [12]. However, in the same study, the authors noted significant and persistent difficulties related to model selection and optimization, leading us to explore automated solutions.

This chapter will serve as a synthesis of current research combining DL and bio-inspired methods applied to the detection of AD. El-Assy *et al.* [13], a dual-CNN model with distinct filters concatenated into a five-output layer (AD, LMCI, MCI, EMCI, and NC) on ADNI data with ADASYN-based class-imbalance correction. It reported up to 99.43%, 99.57%, and 99.30% accuracy for 3-, 4-, and 5-way classification, respectively. Sharma *et al.* [14], the authors obtained accuracy, recall, and F1-scores of 90.4%, 0.905, 0.904, and 0.904, respectively. The dataset was collected using Kaggle. It comprises 6,400 images distributed across two folders (training and test). Each folder is further divided into four subfolders: Mild-Demented, Moderate-Demented, Non-Demented, and VeryMild-Demented. The authors used the VGG-16 architecture as a feature extractor, and another CNN was then used as a classifier (4 outputs).

Certain limitations have been reached within the 2D research community. This has driven the evolution of research towards 3D paradigms. A study published in 2025 introduced the 3D-CNN-VSwinFormer model [15], which combines volume metric convolution with transformer-based attention mechanisms, achieving 92.92% accuracy in distinguishing between patients with AD and healthy individuals. The CNN used in this study was inspired by the model proposed in 2018 by [16], named CBAM for convolutional block attention module. However, the initial model was created for 2D, and since the authors focused on 3D volumes, some modifica-tions had to be made. Regarding the video SwinFormer component, this block uses an attention mechanism based on a 3D sliding window multihead self-attention (MSA).

To conduct their experiment [17], used the ADNI database, specifically the ADNI3 collection. This study is characterized by its output classes: early mild cognitive impairment (EMCI) and normal control (NC), with the objective of early detection of the disease. Initially, they performed pre-processing consisting of registration using the standard MNI152 model and skull extraction using the FMBIR software library (FSL). The data was allocated 80% for training and validation and 20% for testing. This model achieved an accuracy of 81.80%, a recall of 82.50%, and a specificity of 80.50%, thus effectively distinguishing between individuals with mild cognitive impairment (MCI) and those with normal cognitive function (NCF).

With the rise of convolutional neural networks and the difficulties encountered by classical algorithms [18], bio-inspired algorithms have returned to the forefront of the scientific scene as a powerful computational method for exploring complex and multidimensional parameters [19]. These metaheuristics offer robust and adaptive approaches to optimization problems that have proven difficult to solve using traditional methods. In this study [20], for example, the authors combined AIBL and ADNI data in a four-stage framework: fuzzy-logic ROI clustering, feature extraction via PLTP, ResNet-50 and VGG-16, feature selection with the modified gorilla troop optimizer (MGTO), and CapsNet classification. The model reported 99.76%, 99.88%, and 99.92% accuracy for AD vs. NC, MCI vs. AD, and NC vs. MCI, respectively.

A hybrid model combining a convolutional neural network and a spiking neural network (CNN-SNN) was proposed in this study [21]. This hybrid model leverages the spatial feature extraction capabilities of CNNs and the temporal dynamics of SNNs. In other words, the CNN module extracts features from the input image,

while the SNN module processes them over time. According to the authors, this combination allows the model to capture both spatial and temporal information, making it suitable for tasks requiring an understanding of the structure and dynamics of the input data. To highlight the importance of the SNN, the authors conducted an ablation study: its removal reduced accuracy from 99.58% to 75.67%. The preprocessing step consisted of image re-importing, data augmentation, and upsampling (SMOTE [22]).

A 2025 study further confirmed the diagnostic potential of deep CNN architectures for early AD detection from MRI data [23], reinforcing the relevance of convolutional approaches as a solid foundation for AD diagnostic systems. @articlepetersen2010alzheimer, title=Alzheimer's disease Neuroimaging Initiative (ADNI) clinical characterization, author=Petersen, Ronald Carl and Aisen, Paul S and Beckett, Laurel A and Donohue, Michael C and Gamst, Anthony Collins and Harvey, Danielle J and Jack Jr, Clifford R and Jagust, William J and Shaw, Leslie M and Toga, Arthur W and others, journal=Neurology, volume=74, number=3, pages=201–209, year=2010, publisher=Lippincott Williams & Wilkins The integration of convolutional neural networks with bio-inspired optimization algorithms represents an emerging frontier in medical imaging research, though spe-cific applications to AD detection remain relatively underdeveloped. Current literature reveals a gradual but consistent progression toward automated architecture design and optimization, with metaheuristic approaches offering promising pathways to address the well-documented limitations of manually engineered DL models.

## 3. METHOD

### 3.1. Overview of the proposed framework

The proposed methodology integrates CNNs with two bio-inspired algorithms the GA and PSO to automate the design and fusion of DL models for AD classification. As illustrated in Figure 1, the pipeline starts with an essential preprocessing step, followed by three sequential stages: a GA searches for CNN architectures adapted to each anatomical orientation; the optimized models are retrained and validated on a larger, independent dataset to assess generalizability; and finally, PSO determines the fusion weights that combine the predictions from the three anatomical views.

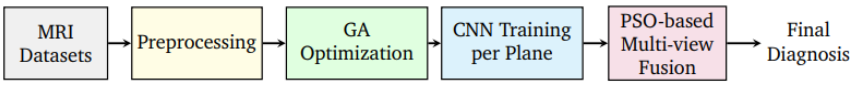


Figure 1. Overall architecture of the proposed CNN-GA-PSO framework

### 3.2. Data acquisition and preprocessing

#### 3.2.1. Datasets

The Kaggle dataset [24] provides 6,400 preprocessed 2D MRI slices (128 × 128 px) distributed across four dementia severity classes, re-labelled into a binary scheme (Demented vs. Non-Demented) for the GA architecture search phase. The ADNI dataset [25] provides 1,715 full 3D structural MRI volumes (823 AD, 892 NC) acquired at 1.5 T and 3 T field strengths, partitioned into training (60%), validation (15%), and held-out test (25%) subsets; subject counts per split are given in Table 1. Two datasets were used across the different stages of this study Table 2.

Table 1. ADNI subject distribution across dataset splits

| Split | AD subjects | NC subjects | Total |
|---|---|---|---|
| Training (60 %) | 494 | 535 | 1,029 |
| Validation (15 %) | 123 | 134 | 257 |
| Test (25 %) | 206 | 223 | 429 |
| Total | 823 | 892 | 1,715 |

Table 2. Summary of datasets used in this study

| Characteristic | ADNI | Kaggle |
|---|---|---|
| Total subjects / images | 1,715 subjects | 6,400 images |
| AD | 823 | 3,200 |
| NC | 892 | 3,200 |
| Data type | 3D volumes | 2D slices |
| Usage | Training, validation, test | GA architecture search |
| Field strength | 1.5 T and 3 T | Unknown |

### 3.2.2. Preprocessing pipeline

Preprocessing MRI images is a critical step in the methodological chain, as the performance of DL models depends heavily on the quality, consistency, and standardization of the input data. Raw MRI volumes exhibit various sources of variability, related to differences in acquisition, scanners, noise, non-homogeneous intensities, and the presence of non-brain structures. To reduce these biases and ensure robust learning, a structured preprocessing pipeline is applied to all volumes. It relies on four main steps: skull stripping, intensity normalization, noise filtering, and inter-subject harmonization.

Skull stripping, also known as brain stripping, involves removing extracerebral structures such as bones, skin, and non-neuronal tissues to focus the analysis exclusively on intracranial regions. A DL model called deepbrain [26], specializing in brain segmentation, was chosen due to its superior accuracy and robustness to inter-subject variation. This approach yields sharp brain masks, preserving cortical and subcortical structures while effectively eliminating non-informative regions.

Intensity Normalization: This step promotes the stability of neural network training and improves the model's ability to generalize to new subjects. It relies on linear stretching of intensities, transforming each voxel according to the minimum and maximum values of the volume. This process unifies intensity distributions and limits the impact of non-biological variations, while preserving internal contrasts between brain tissues.

$$I_{norm} = \frac{I - I_{min}}{I_{max} - I_{min}} \quad (1)$$

Noise filtering and inter-subject harmonization: this noise reduction improves the visual quality of the volumes and enhances the reliability of the features extracted in subsequent steps. The goal is to remove random variations without altering subtle morphological patterns, such as cortical thinning or volumetric variation of the hippocampus, which are key markers of neurodegeneration.

Even after normalization and filtering, residual differences may remain between subjects due to scanners, acquisition centers, or experimental protocols. Inter-subject harmonization is therefore applied to mitigate these discrepancies and standardize the representation of volumes within the dataset. Table 3 reports the average wall-clock time per preprocessing step measured on a representative ADNI volume using Google colab (Tesla T4 GPU).

Table 3. Average wall-clock time per preprocessing step (per MRI volume, Google Colab T4)

| Step | Average time |
|---|---|
| Reorientation and isotropic resampling | 14 s |
| Brain extraction (DeepBrain) | 32 s |
| Intensity normalisation | 3 s |
| Noise filtering | 9 s |
| Inter-subject harmonisation | 7 s |
| 2D slice extraction (per plane) | 4 s |
| Total per subject | ∼1 min 10 s |

## 3.3. Stage 1: Genetic algorithm for CNN architecture optimization

### 3.3.1. Architecture encoding and search space

Each candidate CNN is represented as a chromosome, with genes encoding architectural parameters:

- Number of convolutional-pooling blocks (1-5).
- Kernel sizes (e.g., 3 × 3, 5 × 5) and filter counts per layer (e.g., 32, 64, 128).
- Regularization and optimization parameters: dropout rate (0.2-0.5), optimizer type (Adam and SGD), and activation functions (ReLU and Leaky ReLU).

This search space combines discrete ordinal variables (layer counts and filter sizes) and categorical variables (activation functions, optimizer type), for which gradient-based optimization cannot be applied directly. Exhaustive enumeration is computationally intractable given the combinatorial explosion of configurations, and random search provides no mechanism to direct exploration toward high-fitness regions. GA addresses these con-straints naturally: it operates without gradients, encodes heterogeneous variable types through chromosome representation, maintains population diversity via mutation to avoid premature convergence, and steers the search progressively through selection pressure and crossover recombination.

### 3.3.2. Evolutionary optimization process

The GA begins by initializing a population of random architectures. Each candidate is trained on a subset of the Kaggle dataset, and its validation accuracy serves as the fitness metric. Selection, crossover, and mutation operators are applied iteratively to evolve the population over multiple generations. Selection prioritizes high-fitness individuals; crossover recombines architectural components from parent models; and mutation introduces random variations to maintain diversity. The process terminates when fitness improvement stagnates or a maximum generation count is reached. The optimization workflow is depicted in Figure 2. Table 4 summarises the complete set of hyperparameters governing the GA optimization procedure.

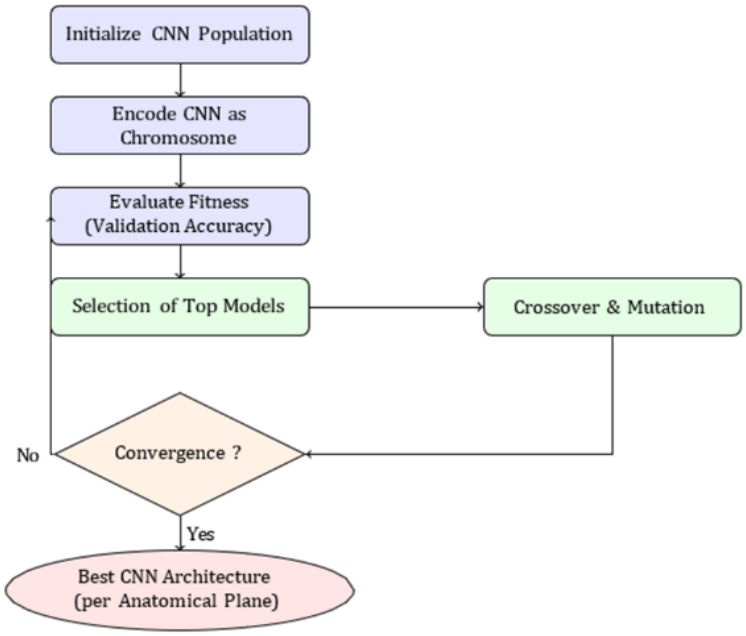


Figure 2. Genetic algorithm optimization workflow for CNN architecture design

Table 4. Hyperparameters of the genetic algorithm for CNN architecture search

| Parameter | Value |
|---|---|
| Population size | 20 |
| Maximum generations | 50 |
| Selection mechanism | Tournament (k = 3) |
| Crossover operator | Uniform crossover |
| Crossover rate | 0.80 |
| Mutation rate | 0.10 |
| Elitism | 2 individuals |
| Training budget per candidate | 10 epochs |
| Training subset (Kaggle) | 6,400 images (128 × 128 px, binary labels) |
| Fitness metric | Validation accuracy |
| Stopping criterion | Max generations or 10 stagnating generations |

### 3.3.3. Orientation-specific architecture search

A unique aspect of this framework is the execution of independent GA runs for axial, coronal, and sagittal MRI planes. This acknowledges that each orientation captures distinct neuroanatomical features and may require specialized feature extraction hierarchies. The best-performing architecture from each orientation is retained for subsequent stages.

### 3.4. Stage 2: CNN training and validation

The architectures optimized by the GA were retrained using 3D MRI data from the ADNI database to evaluate their generalizability to realistic clinical conditions. Figure 3 shows representative coronal, sagittal, and axial slices extracted from these volumes: Figure 3(a) depicts slices from a subject diagnosed with AD, while Figure 3(b) shows the corresponding slices for a cognitively NC.

Each orientation-specific CNN was trained independently for 60 epochs using the Adam optimizer with a learning rate of 1 × 10−4, batch size of 32, and categorical cross-entropy loss. To mitigate overfitting, early stopping (patience = 10 epochs) and learning rate reduction (factor = 0.5) were applied when validation performance plateaued. A subject-independent 5-fold cross-validation scheme ensured no data leakage between training and validation splits. The final model for each view was selected based on the highest mean validation accuracy across folds.

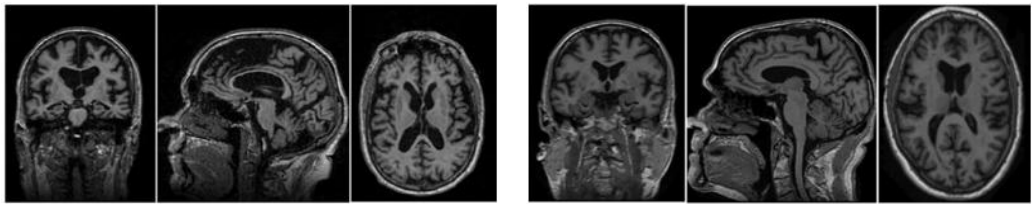

(a) (b)

Figure 3. Representative MRI slices from the ADNI database, illustrating coronal, sagittal, and axial orientations; (a) for both AD patients and (b) healthy controls [27]

### 3.5. Stage 3 multi-view fusion via particle swarm optimization

#### 3.5.1. Fusion motivation and formulation

While each orientation-specific CNN provides valuable discriminatory information, combining their predictions can capture complementary aspects of AD-related neuroanatomical changes. Rather than using uniform averaging, we formulate view fusion as an optimization problem where PSO determines the optimal weighting scheme that maximizes classification accuracy. PSO is selected for this task for two reasons. First, the fitness signal - classification accuracy is a non-differentiable step function of the fusion weights at the decision boundary, which rules out gradient-based optimizers such as Adam or SGD. Second, the sum-to-one constraint $\left(\sum_j wj = 1, w_j \geq 0\right)$ is handled natively by normalizing particle positions after each velocity update, without requiring penalty terms or projection algorithms. These properties make PSO a principled and lightweight choice for this low-dimensional, constrained, non-differentiable optimization problem.

#### 3.5.2. Fusion mechanism

A separate independent dataset of 500 MRI slices-distinct from all data used in previous stages-was utilized to train the PSO fusion module. Each optimized CNN generated probability scores for these slices, forming a matrix $p \sum R^{500x3}$ where columns correspond to axial, coronal, and sagittal predictions, and rows represent slices.

$$p = \begin{bmatrix} p_{1,axial} & p_{1,coronal} & p_{1,sagittal} \\ p_{2,axial} & p_{2,coronal} & p_{2,sagittal} \\ \vdots & \vdots & \vdots \\ p_{500,axial} & p_{500,coronal} & p_{500,sagittal} \end{bmatrix}$$

The PSO algorithm seeks an optimal weight vector,

$$w = [W_{axial,}\, W_{coronal,}\, W_{sagittal}]$$

that satisfies:

$$\omega_{axial} + \omega_{coronal} + \omega_{sagittal} = 1,\ \omega_j \geq 0$$

for each slice $i$, the final fused probability is computed as:

$$\hat{p}_i = \sum_{j=1}^{3} w_j p_{i,j}$$

with the final prediction determined by:

$$\hat{y}_i = \begin{cases} 1, & if\ \hat{p}_i \geq 0.5 \\ 0, & otherwise. \end{cases}$$

### 3.5.3. PSO optimization procedure

Each particle in the swarm represents a candidate weight vector $w^k$. Particle fitness is defined as the classification accuracy on the independent fusion dataset:

$$f(w^k) = 1/N \frac{1}{N} \sum_{i=1}^{N} \mathbb{1}(\hat{y}_i = y_i)$$

at each iteration $t$, particles update their velocity and position according to:

$$v_{k,j}^{(t+1)} = w v_{k,j}^{(t)} + c_1 r_1 \left(p_{k,j}^{best} - w_{k,j}^{(t)}\right) + c_2 r_2 \left(g_j^{best} - w_{k,j}^{(t)}\right)$$

$$w_{k,j}^{(t+1)} = w_{k,j}^{(t)} + v_{k,j}^{(t+1)}$$

where $\omega$ is the inertia weight, $c_1$ and $c_2$ are acceleration coefficients, $r_1, r_2 \sim U(0,1)$ and $g_j^{best}$ represent personal and global best positions, respectively. Weights are normalized after each update to satisfy the constraint.

## 3.6. Implementation details and reproducibility

Table 5 consolidates all hyperparameters and dataset splits required to reproduce the experiments. GA-specific parameters are further detailed in Table 4.

Table 5. Complete hyperparameter and dataset configuration for reproducibility

| Component | Parameter | Value |
|---|---|---|
| Kaggle dataset | Total images | 6,400 (128 × 128 px) |
| | Binary split | Demented: 3,200/non-demented: 3,200 |
| ADNI dataset | AD/NC subjects | 823 AD/892 NC (1,715 total) |
| | Train/Val/Test | 60%/15%/25% (1,029/257/429 subjects) |
| | 2D slices per plane | ~53 400 (training), ~22 300 (test) |
| CNN training (Stage 2) | Epochs | 60 |
| | Optimizer | Adam |
| | Learning rate | $1 \times 10^{-4}$ |
| | Batch size | 32 |
| | Loss function | Categorical cross-entropy |
| | Early stopping | Patience = 10 epochs |
| | LR reduction | Factor 0.5 on plateau |
| | Cross-validation | 5-fold (subject-independent) |
| PSO (Stage 3) | Swarm size $K$ | 30 |
| | Max iterations $T$ | 40 |
| | Inertia weight $\omega$ | 0.7 |
| | Cognitive coeff. $C_1$ | 1.5 |
| | Social coeff. $C_2$ | 1.5 |
| | Fusion dataset size | 500 MRI slices |
| Random seeds | GA/CNN/PSO | 42 (fixed) |

## 3.7. Computational resources

Table 6 reports the computational resources consumed at each stage of the framework. All experiments were conducted on Google Colaboratory, using an NVIDIA Tesla T4 GPU (16 GB VRAM, 70 W TDP) with an Intel Xeon CPU and 12 GB RAM allocated by the platform. The total wall-clock time was approximately 50 hours, distributed across multiple Colab sessions. Estimated energy consumption, derived from the T4's rated TDP, is approximately 50 h × 70 W ≈ 3.5 kWh. The complete end-to-end workflow, from MRI input to final diagnosis and interpretability visualization, is summarized in Figure 4.

Table 6. Computational cost of the proposed framework

| Stage | Candidates/iterations | GPU-hours |
|---|---|---|
| GA — Axial | 20 × 35 = 700 candidates | ~ 9 |
| GA — Coronal | 20 × 38 = 760 candidates | ~ 10 |
| GA — Sagittal | 20 × 41 = 820 candidates | ~ 10 |
| Stage 2 (ADNI, 5-fold) | 5 × 3 = 15 training runs (~53 000 coupes/fold) | ~ 21 |
| PSO fusion | 30 particles × 25 iter | < 0.1 |
| Total | | ~ 50 |

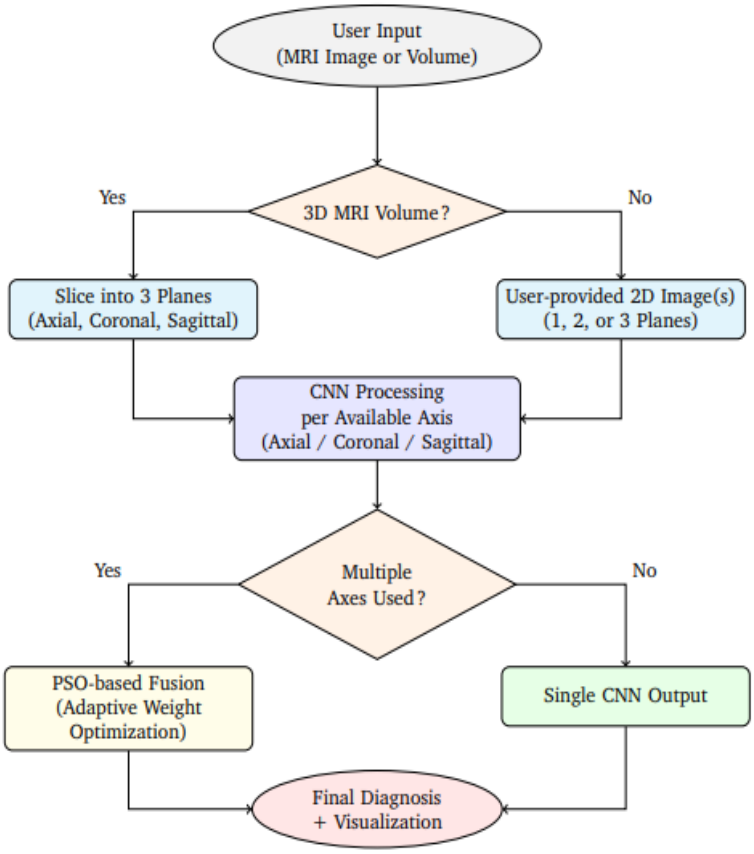


Figure 4. End-to-end workflow of the proposed hybrid framework for AD classification

## 4. RESULT AND DISCUSSION

This section presents a comprehensive evaluation of our CNN-GA-PSO hybrid framework for AD classification. We systematically evaluate each methodological step: CNN architecture optimization using GA, model training on the entire ADNI dataset, and multi-view fusion using PSO. This evaluation relieson quantitative metrics and visual analysis. All experiments address a binary classification task. During the GA architecture search phase, the four-class Kaggle dataset (mild demented: 896, moderate demented: 64, very mild demented: 2,240, non demented: 3,200; total 6,400 images resized to 128 × 128 px) is re-labelled into two balanced categories: demented (mild + moderate + very mild; n = 3,200) versus non demented (n = 3,200). Final retraining and evaluation use the ADNI dataset under the same binary scheme: AD versus cognitively NC. Performance is reported as both aggregate and per-class metrics to characterize model behavior on each diagnostic category.

### 4.1. Genetic algorithm for CNN architecture optimization

#### 4.1.1. Convergence behavior

The GA demonstrated consistent convergence for all three anatomical orientations, albeit along different trajectories. Starting with an accuracy of approximately 49%, all orientations showed steady improvement over generations.

The axial branch reached convergence most rapidly, stabilizing by generation 35 with a final validation accuracy of 75.3%. The coronal orientation required slightly more generations, converging by generation 38 with an accuracy of 73.6%. The sagittal branch exhibited the slowest convergence, reaching stability by generation 41 with an accuracy of 72.4%. This progressive refinement confirms the GA ability to systematically evolve the architecture.

#### 4.1.2. Optimized architectures

The GA-optimized architectures exhibited distinct characteristics tailored to their respective anatomical planes, as summarized in Table 7. The axial architecture, with four convolutional layers and moderate regularization, achieved the highest performance. The coronal model adopted a deeper five-layer structure with stronger regularization, while the sagittal network employed a more compact three-layer

design with mini-mal dropout. These architectural differences reflect the varying complexity of feature extraction required for different anatomical views.

Table 7. Structural parameters and performance of GA-optimized CNN architectures

| Orientation | Filter progression | Dropout rate | Accuracy (%) |
|---|---|---|---|
| Axial | [32, 64, 128, 256] | 0.28 | 75.3 |
| Coronal | [32, 64, 128, 256, 512] | 0.40 | 73.6 |
| Sagittal | [16, 32, 64] | 0.20 | 72.4 |

#### 4.1.3. Performance limitations in optimization phase

The moderate accuracy levels achieved during the GA optimization phase (72.4–75.3%) primarily reflect the computational constraints of evolutionary search. The use of a reduced dataset was necessary to maintain feasible optimization times, as each generation required training and evaluating multiple candidate architectures. Consequently, these accuracies represent architectural potential rather than final performance, with the true capability of the optimized networks becoming apparent only after retraining on the complete ADNI dataset.

### 4.2. Performance evaluation on ADNI dataset

Retraining the genetically optimized architectures on the ADNI dataset resulted in substantial perfor-mance improvements across all orientations. The axial network maintained its superior performance, achieving 85.0% validation accuracy and 84.6% test accuracy. The coronal and sagittal models showed comparable improvement trends, with test accuracies of 83.1% and 82.0% respectively. The consistent performance gap between validation and test metrics (approximately 0.4-0.6 percentage points) indicates effective generalization with minimal overfitting. Table 8 reports the validation accuracy, test accuracy, and validation loss obtained for each orientation-specific model after full retraining on the ADNI dataset.

Table 8. Performance metrics after retraining on ADNI dataset

| Orientation | Val. Acc. (%) | Test Acc. (%) | Val. Loss |
|---|---|---|---|
| Axial | 85.0 | 84.6 | 0.36 |
| Coronal | 83.8 | 83.1 | 0.41 |
| Sagittal | 82.6 | 82.0 | 0.44 |

### 4.3. Multi-view fusion via particle swarm optimization

#### 4.3.1. Convergence and weight distribution

PSO demonstrated efficient convergence, generally reaching stability in 25 iterations with 30 particles and a maximum of 40 iterations. The convergence profile in Figure 5 exhibits two successive phases. During the initial iterations, particles sweep a broad region of the feasible weight space and fitness improves steeply as progressively better fusion configurations are identified.

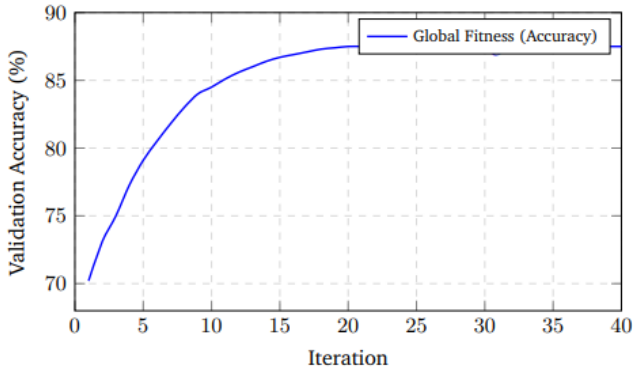


Figure 5. Convergence behavior of PSO optimization for multi-view fusion

This exploratory phase transitions into an exploitation phase around iteration 10, where improvements become increasingly incremental as the swarm contracts toward the global best. A stable plateau is reached at approximately iteration 25-62.5% of the maximum budget - indicating that the swarm of 30 particles locates a high-quality solution well before the iteration limit is reached. The smooth, monotonic progression and the absence of oscillations in the later iterations confirm that the PSO control parameters maintain a productive balance between exploration and exploitation throughout the run. This rapid convergence is consistent with the low effective dimensionality of the problem: the sum-to-one constraint on the three fusion weights reduces the search to a two-dimensional simplex, which is well within the capacity of a moderate-sized swarm. The weight distribution in the last iteration assigns the greatest weight to the axial view (0.46), followed by the coronal (0.33) and sagittal (0.21) views, which corresponds to the individual performance hierarchy of CNNs specific to each orientation. This asymmetric weighting scheme demonstrates the algorithm's ability to quantitatively assess the relative discriminative power of each anatomical view, rather than relying on uniform averaging.

#### 4.3.2. Fusion performance

The PSO-based fusion mechanism yielded significant performance gains. The fused model achieved 87.4% accuracy, representing a 2.8 percentage point improvement over the best individual model (axial CNN). More importantly, the balanced performance across precision (86.8%), recall (87.0%), and F1-score (86.9%) indicates that the fusion mechanism effectively leverages complementary information across views without introducing significant bias.

Table 9 provides a detailed comparison of classification metrics between each individual orientation-specific CNN and the PSO-fused model. To further analyze the performance of the fused model across individual diagnostic categories, Table 10 reports the per-class precision, recall, and F1-score obtained on the ADNI test set. The results demonstrate balanced performance for both NC and AD classes, indicating that the proposed fusion strategy improves overall classification performance without introducing a noticeable bias toward either class.

Table 9. Performance comparison between individual CNNs and PSO-fused model

| Model | Acc. (%) | Prec. (%) | Rec. (%) | F1 (%) | AUC (%) |
|---|---|---|---|---|---|
| Axial CNN | 84.6 | 84.0 | 84.2 | 84.1 | 87.3 |
| Coronal CNN | 83.1 | 82.3 | 81.9 | 82.1 | 86.2 |
| Sagittal CNN | 82.0 | 81.3 | 80.9 | 81.1 | 84.8 |
| PSO fusion | 87.4 | 86.8 | 87.0 | 86.9 | 90.1 |

Table 10. Per-class classification metrics of the PSO-fused model on the ADNI test set

| Class | Precision (%) | Recall (%) | F1-score (%) |
|---|---|---|---|
| NC (Normal control) | 88.4 | 85.2 | 86.8 |
| AD (Alzheimer's) | 85.2 | 88.8 | 87.0 |
| Macro avg. | 86.8 | 87.0 | 86.9 |

### 4.4. Visual Interpretation via Gradient-weighted CAM

Applying gradient-weighted class activation mapping (Grad-CAM) provided a better understanding of the model's decision-making process. Grad-CAM was applied to the last convolutional block of each GA-optimized CNN-the fourth, fifth, and third block for the axial, coronal, and sagittal networks, respectively Table 7 immediately prior to the global average pooling operation. This choice is standard practice: the last convolutional layer retains the richest semantic content while preserving sufficient spatial resolution for meaningful localization - earlier layers capture low-level textures but lack discriminative power, while post-pooling layers discard spatial information entirely. From the 128 × 128 input, these blocks produce activation maps of 8 × 8, 4 × 4, and 16 × 16 for the axial, coronal, and sagittal models, which were bilinearly upsampled to the input resolution and overlaid on the slice for visual interpretation. Figure 6 illustrates representative visualizations for both correct and incorrect classifications. In false negative cases (Figure 6(a)), the model exhibited diffuse and poorly localized activation patterns, suggesting the model's uncertainty when discriminating features were less pronounced. In contrast, in true positive cases (Figure 6(b)), the model consistently focused on regions of medical interest, including the medial temporal lobe and hippocampus, regions clinically associated with AD pathology. These visualizations not only enhance interpretability but also provide clinical validation by demonstrating that the model's attention aligns with known neuropathological markers of AD.

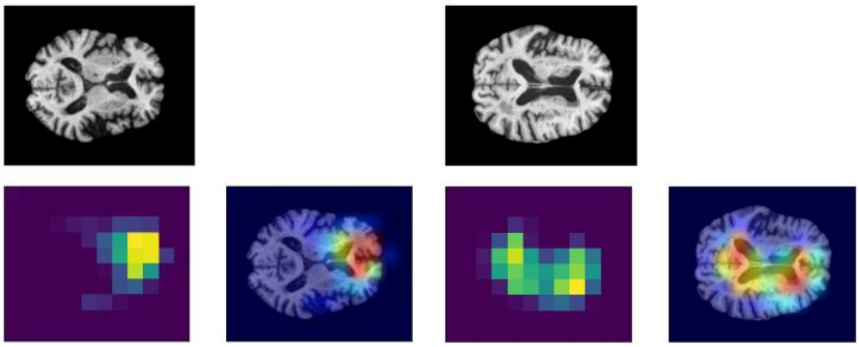

(a) (b)

Figure 6. Grad-CAM visualizations illustrating model attention patterns; (a) false negative case with diffuse activation pattern and (b) true positive case with focused hippocampal activation

### 4.5. Failure mode analysis

Figure 7 presents the confusion matrices at each stage of the framework, evaluated on their respective test sets. The progression across the three stages reveals a consistent reduction in classification errors. The GA phase Figure 7(a), operating on the Kaggle dataset (N = 960), produces 237 total errors (119 FP, 118 FN), reflecting the architectural search constraints of models trained on limited 2D data. After retraining on the larger ADNI cohort Figure 7(b) N = 429 subjects, 206 AD and 223 NC), total errors drop to 66 (37 FP, 29 FN), confirming the benefit of training on a clinically representative 3D dataset. The PSO fusion stage Figure 7(c); N = 500) achieves the lowest error count of 65 (37 FP, 28 FN), with the most notable improvement in false negatives - the clinically critical error type where AD cases go undetected. The 28 remaining false negatives are consistent with the diffuse Grad-CAM activation patterns in Figure 6(a), characteristic of borderline atrophy cases where 2D projections capture insufficient spatial context. The slight asymmetry (FN < FP) reflects a conservative tendency toward AD prediction, which is preferable in a screening context.

| | | Pred. | |
|---|---|---|---|
| | | **NC** | **AD** |
| **Act.** | NC | **361** | 119 |
| | AD | 118 | **362** |

(a)

| | | Pred. | |
|---|---|---|---|
| | | **NC** | **AD** |
| **Act.** | NC | **186** | 37 |
| | AD | 29 | **177** |

(b)

| | | Pred. | |
|---|---|---|---|
| | | **NC** | **AD** |
| **Act.** | NC | **213** | 37 |
| | AD | 28 | **222** |

(c)

Figure 7. Confusion matrices at each stage of the framework (rows: actual; columns: predicted) (a) GA phase, axial (75.3%), Kaggle (N = 960), (b) ADNI retraining, axial (84.6%), N = 429, and (c) PSO fusion (87.4%), N = 500

### 4.6. Statistical analysis

To assess the reliability of the reported results, 95% confidence intervals (CI) were computed using the normal approximation - for the individual CNNs on the ADNI test set (N = 429) and for the fused model on the fusion evaluation set (N = 500) - and Cohen's κ was derived from the confusion matrices to quantify agreement beyond chance, as summarized in Table 11.

$$CI_{95\%} = \hat{p} \pm 1.96\sqrt{\frac{\hat{p}(1-\hat{p})}{N}} \quad (2)$$

Table 11. Statistical evaluation of classification models

| Model | Accuracy (%) | 95% CI | Cohen's $\kappa$ | Interpretation |
|---|---|---|---|---|
| Axial CNN | 84.6 | [81.2, 88.0] | 0.69 | Substantial |
| Coronal CNN | 83.1 | [79.6, 86.7] | 0.66 | Substantial |
| Sagittal CNN | 82.0 | [78.4, 85.6] | 0.64 | Substantial |
| PSO fusion | 87.4 | [84.5, 90.3] | 0.74 | Substantial |

The fused model's point estimate (87.4%) exceeds that of every individual CNN, although its confidence interval partially overlaps with that of the axial baseline ([81.2, 88.0]); the gain of 2.8 percentage points should therefore be read as indicative rather than as a formally significant difference on this sample size. Cohen's κ rises from 0.69 for the best individual CNN to 0.74 for the fused model, a change consistent with the improved recall for the AD class observed in Table 10. The consistency between validation accuracy (85.0%) and test accuracy (84.6%) for the axial model across the 5-fold cross-validation scheme further suggests stable generalisation with no evidence of overfitting. A formal McNemar's test comparing PSO fusion against the axial baseline would require access to the per-sample prediction vectors from both models on the same test set; these results, while not reported here, can be readily obtained from the stored model outputs.

### 4.7. Comparison with state-of-the-art methods

Table 12 positions the proposed framework against representative recent approaches for AD classification from structural MRI. Because methods vary substantially in dataset, classification task, and input dimensionality, a "Task/Dataset" column is included to support a fair reading of the accuracy figures.

Table 12. Comparison with state-of-the-art methods for AD classification from MRI

| Method | Architecture | Dataset | Task | Acc. (%) |
|---|---|---|---|---|
| Sharma *et al.* [14] | VGG-16 (2D) | Kaggle | 4-class | 90.4 |
| El-Assy *et al.* [13] | Dual CNN (2D) | ADNI | 3-class/5-class | 99.4/99.3 |
| Woo *et al.* [17] | 3D CNN | ADNI | EMCI vs NC (binary) | 81.8 |
| Zhou *et al.* [15] | 3D CNN + VSwinFormer | ADNI | AD vs NC (binary) | 92.9 |
| Ganesan *et al.* [20] | ResNet-50 + VGG-16 + CapsNet | AIBL + ADNI | AD vs NC (binary) | 99.8 |
| Slimi *et al.* [21] | CNN-SNN hybrid (2D) | Kaggle | 2-class | 99.6 |
| Proposed | GA-PSO + 2D CNN (multi-view) | ADNI | AD vs NC (binary) | 87.4 |

Several observations arise from this comparison. Methods operating on the Kaggle dataset [14], [21] or using multi class ADNI setups [13], [20] benefit from either a curated, pre-segmented image collection or a classification scheme in which class boundaries are more discriminable, explaining the higher accuracy figures. Among approaches that address the binary AD vs. NC problem on ADNI volumetric data the most clinically relevant and challenging configuration - Zhou *et al.* [15] achieve 92.9% with a 3D-CNN hybrid exploiting full volumetric context, while Woo *et al.* [17] report 81.8% for the related EMCI vs. NC task. The proposed framework reaches 87.4% within this direct comparison bracket through plane-wise 2D processing and automated architecture design rather than hand-crafted 3D feature extractors. Here the 2D representation is not a fallback but the basis of the multi-view fusion strategy, since it is the decomposition into anatomical planes that yields the separate views combined by PSO. The 5.5 percentage-point gap with respect to Zhou *et al.* [15] is the counterpart of this design: part of the volumetric context exploited by 3D networks remains inaccessible to plane-wise models - a limitation discussed in section 4. The key contribution of the proposed method lies not in surpassing absolute accuracy records but in the end-to-end automation of both architecture design (GA) and multi-view fusion (PSO), which reduces reliance on expert-driven hyperparameter choices.

### 4.8. Discussion

The staged performance progression-from moderate GA-phase accuracy to substantial gains after ADNI retraining, and the best results through PSO fusion-validates the step-by-step design of the framework. The Grad-CAM visualizations further reinforce confidence by showing that model attention falls on anatomically plausible regions, addressing the need for interpretability in medical AI. Despite these encouraging results, the study presents several limitations that should be considered when interpreting the findings. The 2D slice representation is a deliberate design foundation rather than a mere shortcut: decomposing each volume into axial, coronal, and sagittal planes is what creates the distinct views that the PSO fusion mechanism weights and combines. This design, additionally favoured by its lower computational cost within the GA loop, nonetheless carries an intrinsic cost of its own - each plane captures only a partial projection of inter-slice spatial context. Since morphological markers of neurodegeneration such as hippocampal atrophy are inherently three-dimensional, part of their volumetric signal is not directly accessible to plane-wise networks. This may explain the remaining gap between the fused model's accuracy (87.4%) and the near-perfect scores reported by some 3D DL approaches in the literature. Second, the evaluation is conducted exclusively on ADNI data, a highly standardized research cohort

acquired under controlled imaging protocols. Performance may degrade when the model is applied to images from heterogeneous clinical scanners, different acquisition parameters, or patient populations underrepresented in ADNI (e.g., non-Western demographics, patients with comorbidities). Third, the binary AD vs. NC framing represents the most favorable classification scenario; dis-tinguishing intermediate cognitive stages - such as early or late MCI - is substantially harder and is not evaluated here. These limitations point to concrete directions for strengthening the framework in future work.

## 5. CONCLUTION

In this study, we proposed a GA-PSO hybridization for the automated design of CNN architectures and multi-view fusion in AD classification from MRI data. The PSO-fused model reached 87.4% accuracy (86.9% F1-score, 90.1% AUC), outperforming any single-view CNN, while Grad-CAM confirmed that its attention aligns with clinically relevant regions such as the hippocampus. The results are encouraging, yet several limitations must be acknowledged. First, the framework is built on a 2D slice representation, which is what enables the very multi-view fusion at the heart of the method - each anatomical plane forms a separate view to be weighted by PSO - and which is further favoured by its lower computational cost within the GA loop; the counterpart is that plane-wise processing discards part of the inter-slice spatial context that volumetric CNN architectures would capture more faithfully. Second, the evaluation relies on the ADNI dataset, a carefully curated research cohort that may not reflect the scanner diversity, protocol variability, and demographic heterogeneity of routine clinical settings multi-center prospective validation remains necessary before any clinical deployment can be considered. Third, the binary classification setting (AD vs. NC) does not cover the full diagnostic continuum, and performance on intermediate stages such as MCI warrants dedicated investigation. Future work will explore 3D CNN architectures within the GA search space, extension to multi-class AD staging, and integration of complementary modalities (PET and fMRI) to close the gap between research prototypes and clinically deployable diagnostic tools.

## ACKNOWLEDGMENTS

The authors thank their colleagues at the SIMPA laboratory and the Lens Computer Science Research Center for their fruitful exchanges and IT support throughout this project.

## FUNDING INFORMATION

This research received no specific funding from public, commercial, or non-profit organizations.

## AUTHOR CONTRIBUTIONS STATEMEN

This journal uses the Contributor Roles Taxonomy (CRediT) to recognize individual author contributions, reduce authorship disputes, and facilitate collaboration.

| Name of Author | C | M | So | Va | Fo | I | R | D | O | E | Vi | Su | P | Fu |
|---|---|---|---|---|---|---|---|---|---|---|---|---|---|---|
| Iheb Chemss El Dine | ✓ | ✓ | ✓ | ✓ | ✓ | ✓ | | ✓ | ✓ | ✓ | ✓ | | | |
| Nacéra Benamrane | ✓ | ✓ | | ✓ | | | | ✓ | | | ✓ | ✓ | ✓ | |
| Lakhdar Sais | | | | ✓ | | | | | | | ✓ | ✓ | | |

C : **C**onceptualization
M : **M**ethodology
So : **So**ftware
Va : **Va**lidation
Fo : **Fo**rmal analysis
I : **I**nvestigation
R : **R**esources
D : **D**ata Curation
O : Writing - **O**riginal Draft
E : Writing - Review & **E**diting
Vi : **Vi**sualization
Su : **Su**pervision
P : **P**roject administration
Fu : **Fu**nding acquisition

## CONFLICT OF INTEREST STATEMENT

The authors declare that there are no financial interests, commercial affiliations, or other potential conflicts of interest that could have influenced the objectivity of this research or the writing of this paper.

## DATA AVAILABILITY

The data supporting this study are available from the following sources:

- Kaggle Dataset: The Augmented Alzheimer MRI Dataset dataset used in this study is publicly available in the Kaggle repository at https://www.kaggle.com/datasets/uraninjo/augmented-alzheimer-mri-dataset.
- ADNI Data: The Alzheimer's Disease Neuroimaging Initiative (ADNI) data that support the findings of this study are available from a third party. These data were obtained under a data use agreement and are not publicly available. However, they can be requested by qualified researchers through the official ADNI data access process.

The code developed for this study is available from the corresponding author upon request.

## REFERENCES


[1] K. O'Shea and R. Nash, "An introduction to convolutional neural networks." Dec. 02, 2015. [Online]. Available: http://arxiv.org/abs/1511.08458

[2] M. A. K. Raiaan *et al.*, "A systematic review of hyperparameter optimization techniques in convolutional neural networks," *Decision Analytics Journal*, vol. 11, p. 100470, Jun. 2024, doi: 10.1016/j.dajour.2024.100470.

[3] Z. Li, K. Kamnitsas, and B. Glocker, "Analyzing overfitting under class imbalance in neural networks for image segmentation," *IEEE Transactions on Medical Imaging*, vol. 40, no. 3, pp. 1065–1077, Mar. 2021, doi: 10.1109/TMI.2020.3046692.

[4] A. Kharrat and M. Néji, "Classification of brain tumors using personalized deep belief networks on MRImages: PDBN-MRI," in *Eleventh International Conference on Machine Vision (ICMV 2018)*, D. P. Nikolaev, P. Radeva, A. Verikas, and J. Zhou, Eds., SPIE, Mar. 2019, p. 38. doi: 10.1117/12.2522848.

[5] W. R. Drioua, N. Benamrane, and L. Sais, "Breast cancer histopathological images segmentation using deep learning," *Sensors*, vol. 23, no. 17, p. 7318, Aug. 2023, doi: 10.3390/s23177318.

[6] J. H. (John H. Holland and J. H, *Adaptation in natural and artificial systems : an introductory analysis with applications to biology, control, and artificial intelligence*. 1992.

[7] N. Benamrane and A. Fekir, "Medical images segmentation by neuro-genetic approach," in *Proceedings of the International Conference on Information Visualisation*, 2005, pp. 981–986. doi: 10.1109/IV.2005.78.

[8] A. Slowik, "Particle Swarm Optimization," in *The Industrial Electronics Handbook - Five Volume Set*, Boston, MA: IEEE, 2011, pp. 1942–1948. doi: 10.1007/978-3-319-46173-1_2.

[9] A. Kharrat, N. Benamrane, M. B. Messaoud, and M. Abid, "Genetic algorithm for feature selection of MR brain images using wavelet co-occurence," in *International Conference on Graphic and Image Processing (ICGIP 2011)*, Oct. 2011, p. 828557. doi: 10.1117/12.913381.

[10] M. Lazreg and N. Benamrane, "Hybrid system for optimizing the robot mobile navigation using ANFIS and PSO," *Robotics and Autonomous Systems*, vol. 153, p. 104114, Jul. 2022, doi: 10.1016/j.robot.2022.104114.

[11] I. C. El-Dine-Hagani and N. Benamrane, "Alzheimer disease detection using convolutional neural network and particle swarm optimization," in *2024 5th International Conference on Electronic Engineering and Signal Processing (EESP)*, IEEE, Dec. 2024, pp. 30–34. doi: 10.1109/EESP64500.2024.00014.

[12] M. G. Alsubaie, S. Luo, and K. Shaukat, "Alzheimer's disease detection using deep learning on neuroimaging: a systematic review," *Machine Learning and Knowledge Extraction*, vol. 6, no. 1, pp. 464–505, 2024, doi: 10.3390/make6010024.

[13] A. M. El-Assy, H. M. Amer, H. M. Ibrahim, and M. A. Mohamed, "A novel CNN architecture for accurate early detection and classification of Alzheimer's disease using MRI data," *Scientific Reports*, vol. 14, no. 1, p. 3463, Feb. 2024, doi: 10.1038/s41598-024-53733-6.

[14] S. Sharma, K. Guleria, S. Tiwari, and S. Kumar, "A deep learning based convolutional neural network model with VGG16 feature extractor for the detection of Alzheimer Disease using MRI scans," *Measurement: Sensors*, vol. 24, p. 100506, Dec. 2022, doi: 10.1016/j.measen.2022.100506.

[15] J. Zhou *et al.*, "A deep learning model for early diagnosis of alzheimer's disease combined with 3D CNN and video swin transformer," *Scientific Reports*, vol. 15, no. 1, p. 23311, Jul. 2025, doi: 10.1038/s41598-025-05568-y.

[16] Zia-Ur-Rehman, M. K. Awang, G. Ali, and M. Faheem, "Recent advancements in neuroimaging-based Alzheimer's disease prediction using deep learning approaches in e-health: a systematic review," *Health Science Reports*, vol. 8, no. 5, May 2025, doi: 10.1002/hsr2.70802.

[17] S. Woo, J. Park, J.-Y. Lee, and I. S. Kweon, "CBAM: convolutional block attention module." Jul. 18, 2018. [Online]. Available: http://arxiv.org/abs/1807.06521

[18] P. Abbasian and T. A. Hammond, "A comprehensive analysis of early Alzheimer disease detection from 3D sMRI images using deep learning frameworks," *Information*, vol. 15, no. 12, p. 746, Nov. 2024, doi: 10.3390/info15120746.

[19] M. G. Alsubaie, S. Luo, and K. Shaukat, "Alzheimer's disease detection using deep learning on neuroimaging: a systematic review," *Machine Learning and Knowledge Extraction*, vol. 6, no. 1, pp. 464–505, Feb. 2024, doi: 10.3390/make6010024.

[20] P. Ganesan, G. P. Ramesh, C. Puttamdappa, and Y. Anuradha, "A modified bio-inspired optimizer with capsule network for diagnosis of Alzheimer disease," *Applied Sciences*, vol. 14, no. 15, p. 6798, Aug. 2024, doi: 10.3390/app14156798.

[21] H. Slimi, I. Cherif, S. Abid, and M. Sayadi, "Biologically inspired hybrid model for Alzheimer's disease classification using structural MRI in the ADNI dataset," *Frontiers in Artificial Intelligence*, vol. 8, Jun. 2025, doi: 10.3389/frai.2025.1590599.

[22] N. V. Chawla, K. W. Bowyer, L. O. Hall, and W. P. Kegelmeyer, "SMOTE: synthetic minority over-sampling technique," *Journal of Artificial Intelligence Research*, vol. 16, pp. 321–357, Jun. 2002, doi: 10.1613/jair.953.

[23] S. Dardouri, "An efficient method for early Alzheimer's disease detection based on MRI images using deep convolutional neural networks," *Frontiers in Artificial Intelligence*, vol. 8, Apr. 2025, doi: 10.3389/frai.2025.1563016.

[24] "Alzheimer MRI preprocessed dataset," Kaggle. Accessed: Apr. 07, 2026. [Online]. Available: https://www.kaggle.com/datasets/uraninjo/augmented-alzheimer-mri-dataset

[25] R. C. Petersen *et al.*, "Alzheimer's Disease Neuroimaging Initiative (ADNI): Clinical characterization," *Neurology*, vol. 74, no. 3, pp. 201–209, Jan. 2010, doi: 10.1212/WNL.0b013e3181cb3e25.

[26] I. Itzcovich, "Deepbrain," Itzco. Accessed: Apr. 07, 2026. [Online]. Available: https://github.com/iitzco/deepbrain

[27] S. Mishra, I. Beheshti, M. Tanveer, and P. Khanna, "3D Supervoxel based features for early detection of AD: a microscopic view to the brain MRI," *Multimedia Tools and Applications*, vol. 81, no. 16, pp. 22481–22496, Jul. 2022, doi: 10.1007/s11042-021-11871-3.

## BIOGRAPHIES OF AUTHORS

**Iheb Chemss El Dine Hagani** received his M.Sc. degree in Computer Science from the University of Sciences and Technology of Oran – Mohamed Boudiaf (USTO-MB), Algeria. He is currently a Ph.D. candidate at SIMPA Laboratory, USTO-MB. His research interests include machine learn-ing, deep learning for medical imaging, bio-inspired optimization algorithms, and clinical decision support systems. He can be contacted at email: ihebchemsseldine.hagani@univ-usto.dz.

**Nacéra Benamrane** received her engineering degree in Computer Science from University of Oran Es-Senia, Algeria, the M.Sc. and Ph.D. degrees from Polytechnic University of Hauts de-France, France. Since 2017, professor Nace´ra Benamrane is a director of SIMPA laboratory in Computer Science department at University of Science and Technology of Oran-Mohamed Boudiaf (USTO-MB). Her main research interests include image processing, medical imaging, computer vision, biomedical engineering, pat-tern recognition and bioinformatics. She can be contacted at email: nacera.benamrane@univ-usto.dz.

**Lakhdar Sais** obtained a Ph.D. in 1993 from the Aix-Marseille University and an "Habilitation a` Diriger des Recherches" from "Universite´ d'Artois" in 2000. In 1994, he joined the IUT of Lens as a lecturer and has actively participated in the development of the Lens computer science research Lab (CRIL) since its creation. Before his current position as a professor at CRIL–CNRS, he spent one year as a professor at IRIT "Universite´ Toulouse III - Paul Sabatier". He spent two years as a researcher at INRIA Lille Nord Europe and CNRS. He was the leader (from 2002 - 2013) of the inference and decision process research group at CRIL. He was the Delegate director of the CRIL laboratory (2013-2018). His research focuses on search and representation problems in Artificial Intelligence. He is especially interested in propositional satisfiability, quantified boolean formula, constraint programming and operation research, knowledge representation and reasoning, data mining, AI, and Social and Human Sciences. He can be contacted at email: sais@cril.fr.